

# Y<sup>3+</sup> substituted Sr-hexaferrites: sol-gel synthesis, structural, magnetic and electrical characterization

*(Hexaferritas de Sr com Y<sup>3+</sup>: síntese sol-gel, caracterização estrutural, magnética e elétrica)*

S. S. Satpute<sup>1</sup>, S. R. Wadgane<sup>2</sup>, S. R. Kadam<sup>1</sup>, D. R. Mane<sup>3</sup>, R. H. Kadam<sup>1\*</sup>

<sup>1</sup>Shrikrishna Mahavidyalaya, Gunjoti, Materials Science Research Laboratory, Osmanabad (M.S.), India

<sup>2</sup>Dhole Patil College of Engineering, Physics Department, Wagholi, Pune (M.S.), India

<sup>3</sup>Government of Maharashtra, Department of Higher Education, Pune (M.S.), India

## Abstract

Y<sup>3+</sup> substituted strontium hexaferrites having chemical composition SrY<sub>x</sub>Fe<sub>12-x</sub>O<sub>19</sub> (x=0.0, 0.5, 1.0, 1.5) were successfully synthesized by sol-gel auto-combustion method. The structural and morphological studies of prepared samples were investigated by using X-ray diffraction technique, energy dispersive X-ray spectroscopy, field emission scanning electron microscopy (FE-SEM) and high-resolution transmission electron microscopy. The X-ray diffraction pattern confirmed the single-phase hexagonal structure of yttrium substituted strontium ferrite and the lattice parameters a and c increased with the substitution of Y<sup>3+</sup> ions. The crystallite size also varied with x content from 60 to 80 nm. The morphology was studied by FE-SEM, and the grain size of nanoparticles ranged from 44 to 130 nm. The magnetic properties were investigated by using vibrating sample magnetometer. The value of saturation magnetization decreased from 49.60 to 35.40 emu/g. The dielectric constant decreased non-linearly whereas the electrical dc resistivity increased with the yttrium concentration in strontium hexaferrite.

**Keywords:** sol-gel, XRD, FE-SEM, HR-TEM, VSM, dielectric constant.

## Resumo

Hexaferritas de estrôncio com adição de Y<sup>3+</sup> com composição química SrY<sub>x</sub>Fe<sub>12-x</sub>O<sub>19</sub> (x= 0,0, 0,5, 1,0, 1,5) foram sintetizadas com sucesso pelo método sol-gel com autocombustão. Os estudos estruturais e morfológicos das amostras preparadas foram investigados usando a técnica de difração de raios X, espectroscopia de energia dispersiva, microscopia eletrônica de varredura com emissão de campo (MEV-FEG) e microscopia eletrônica de transmissão de alta resolução. O padrão de difração de raios X confirmou a estrutura hexagonal monofásica da ferrita de estrôncio substituída com ítrio e os parâmetros de rede a e b aumentaram com a substituição dos íons Y<sup>3+</sup>. O tamanho do cristalito também variou com o teor de x de 60 a 80 nm. A morfologia foi estudada por MEV-FEG e o tamanho de grão das nanopartículas variou de 44 a 130 nm. As propriedades magnéticas foram investigadas usando magnetômetro de amostra vibrante. O valor da magnetização de saturação diminuiu de 49,60 para 35,40 emu/g. A constante dielétrica diminuiu de forma não linear, enquanto a resistividade elétrica CC aumentou com a concentração de ítrio na hexaferrita de estrôncio.

**Palavras-chave:** sol-gel, DRX, MEV-FEG, MET-AR, VSM, constante dielétrica.

## INTRODUCTION

In the last few decades, the pure and doped strontium hexaferrite have attracted much attention due to their electrical and magnetic properties and their applications in microwave devices, recording media, signal processing devices and permanent magnet [1]. Strontium hexaferrite has large saturation magnetization (Ms), high coercivity (Hc), high value of resistivity and superior chemical stability; hence, it has been used as a permanent magnet [2]. The strontium hexaferrite has a hexagonal structure

and crystallographic p63/mmc space group [3]. It consists of 64 ions in a unit cell which occupy on 11 different sites. The 24 Fe<sup>3+</sup> ions occupy on five different sites out of which three are at octahedral (12k, 2a, and 4f2), one of which is at tetrahedral (4f1) and one is at trigonal bipyramidal (2b) [4]. The strontium hexaferrite is synthesized by various techniques and substitutions of different types of ions strongly affect their structural, morphological, magnetic and electrical properties. The substitutions of various types of ions are distributed in octahedral, tetrahedral and trigonal bipyramidal sites [5]. In the microwave application, the material should possess a high resistivity [6]. The magnetic and electrical properties of strontium hexaferrite can be modified with the substitution of suitable cations, so many

\*ram111612@yahoo.co.in

 <https://orcid.org/0000-0001-6973-6938>

researchers carried out studies by doping different ions and make it suitable for the application in various fields [7, 8]. The Fe substitution of  $\text{SrFe}_{12-x}\text{Al}_x\text{O}_{19}$  hexaferrite synthesized by the citrate precursor method shows that saturation magnetization decreases whereas coercivity increases with the substitution of  $\text{Al}^{3+}$  ions in ferrite caused by the small size of crystallite and defect in lattice parameter [9]. It is found that the dc electrical resistivity increases with the lanthanum concentration and its order of magnitude is 109  $\Omega\cdot\text{cm}$  [10]. The  $\text{Ca}_x\text{Sr}_{1-x}\text{Fe}_{12}\text{O}_{19}$  shows that the values of dielectric constant ( $\epsilon'$ ) and dielectric loss tangent ( $\tan\delta$ ) are in good agreement with the dc electrical resistivity [11]. The effect of  $\text{Y}^{3+}$  ions substituted in strontium ferrite having chemical composition  $\text{SrY}_x\text{Fe}_{12-x}\text{O}_{19}$  for ( $x = 0, 0.5, 1, 1.5$ ) was successfully synthesized by the sol-gel auto combustion technique. The aim of present research is to investigate the effect of substitution of  $\text{Y}^{3+}$  on structural, morphological, magnetic, dielectric and electrical properties of strontium hexaferrite and its applications in different fields.

## EXPERIMENTAL

**Materials:** the sol-gel auto-combustion method [11] was used to synthesize the  $\text{Y}^{3+}$  ions substituted in strontium hexaferrite having formula  $\text{SrY}_x\text{Fe}_{12-x}\text{O}_{19}$  for  $x = 0, 0.5, 1.0, 1.5$ . The nanoparticles of  $\text{Y}^{3+}$  substituted strontium hexaferrite consisted of starting material of AR grade strontium nitrate  $\text{Sr}(\text{NO}_3)_2$  (Sigma-Aldrich, 99.9%), ferric nitrate  $\text{Fe}(\text{NO}_3)_3\cdot 9\text{H}_2\text{O}$  (Acros, 99.9%), yttrium nitrate  $\text{Y}(\text{NO}_3)_3\cdot 9\text{H}_2\text{O}$  (Sigma-Aldrich, 99.9%), citric acid monohydrate (Acros, 99.9%); all mentioned nitrates were mixed with each other according to their proportional quantity.

**Sample preparation:** all nitrates were dissolved in 150 mL distilled water for uniform mixing and placed on a magnetic stirrer with a hot plate at 80 °C. The solution was stirred continuously and citric acid was added into nitrate solution having the molar ratio 1:3. In order to maintain the pH value of about 7, ammonia was added dropwise in the solution. After 3-4 h gel formation took place. The viscous brown gel was placed on a hot plate at 150 °C; after some time, the combustion took place and the fine powder of yttrium substituted strontium hexaferrite was obtained. The sample was pre-sintered at 600 °C for 4 h in muffle furnace then it was cooled up to room temperature. The sintered powders were ground for 2 h in order to obtain a uniform mixture of ferrite. The samples were finally sintered at 1000 °C for 6 h where final products in the form of crystalline nanoparticles were obtained. The pellets of the prepared samples with a diameter of 10 mm and a thickness of 1 mm were formed using a uniaxial hydraulic pressing machine, where PVA was used as a binder. The prepared pellets were finally sintered at 1000 °C in a muffle furnace for 6 h.

**Characterization:** to study the structure of prepared samples, X-ray diffraction technique (Ultima-IV, Rigaku) was used. X-ray diffraction patterns were recorded at room temperature in the  $2\theta$  range from 20° to 80° using  $\text{CuK}\alpha$

radiation ( $\lambda = 1.5404 \text{ \AA}$ ). The elemental composition of  $\text{SrY}_x\text{Fe}_{12-x}\text{O}_{19}$  samples was studied using the energy dispersive X-ray analysis (EDAX). The surface morphology of the sample was studied using a field emission scanning electron microscope (FE-SEM, JSM-6360). The high-resolution transmission electron microscope (HR-TEM, FEI, Tecnai J2, F30) was used to determine the grain size and interplanar spacing of the prepared samples. The magnetic properties were studied using a vibrating sample magnetometer (VSM) by applying 1.5 tesla magnetic field at room temperature. The dielectric properties such as dielectric constant and dielectric loss were measured with the help of LCR-Q meter with varying frequency. The electrical dc resistivity was measured as a function of temperature with the help of the two-probe measurement technique.

## RESULTS AND DISCUSSION

**Structural analysis:** Fig. 1 shows the X-ray diffraction (XRD) patterns of  $\text{SrY}_x\text{Fe}_{12-x}\text{O}_{19}$  samples sintered at 1000 °C for  $x = 0, 0.5, 1, 1.5$ . All diffraction peaks of obtained XRD patterns fairly matched the standard peaks without any impurity. The diffraction peaks were recorded with angle  $2\theta$  in the range 20°-80°. The positions of all peaks recorded of planes (110), (107), (114), (203), (205), (206), (217), (201), (211), (220) and (317) were indexed according to the standard diffraction pattern of hexagonal ferrite (JCPDS 80-1197). The yttrium concentration showed a noticeable effect on diffraction peak intensity for (114) and (107) planes. The X-ray diffraction confirmed the hexagonal structure of the samples. The values of lattice constants  $a$  and  $c$  were calculated by standard relation [12]. It was observed that the values of lattice parameter  $a$  (5.878 Å) and  $c$  (23.050 Å) increased in the composition with increasing yttrium concentration in strontium hexaferrite. This can be attributed to the difference in the ionic radii of  $\text{Y}^{3+}$  (0.9 Å) and  $\text{Fe}^{3+}$  (0.63 Å) [13]. The ratio of lattice parameters  $c/a$  decreased with increasing yttrium

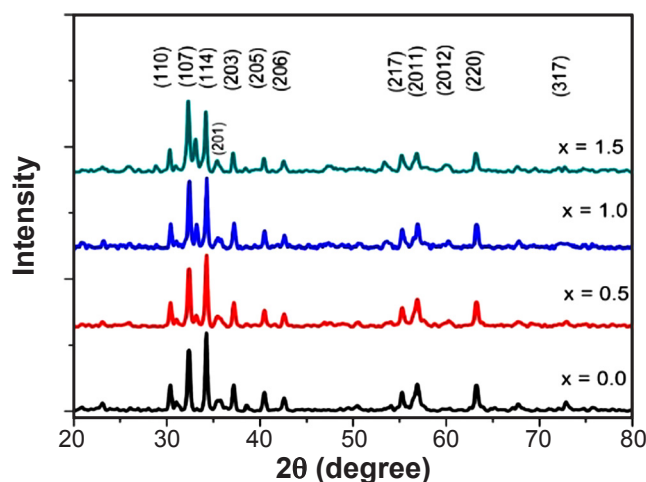


Figure 1: XRD patterns of  $\text{SrY}_x\text{Fe}_{12-x}\text{O}_{19}$  for different substitution level of yttrium.

[Figura 1: Padrões de DRX de  $\text{SrY}_x\text{Fe}_{12-x}\text{O}_{19}$  para diferentes níveis de substituição de ítrio.]

Table I - Structural properties of  $\text{SrY}_x\text{Fe}_{12-x}\text{O}_{19}$  nanoparticles.  
 [Tabela I - Propriedades estruturais das nanopartículas de  $\text{SrY}_x\text{Fe}_{12-x}\text{O}_{19}$ .]

Conc. x	Lattice parameter		c/a ratio	$V_{\text{Cell}}$ ( $\text{\AA}^3$ )	Crystallite size (nm)	X-ray density ( $\text{g/cm}^3$ )	Bulk density ( $\text{g/cm}^3$ )	Porosity (%)	Specific surface area ( $\text{m}^2/\text{g}$ )
	a ( $\text{\AA}$ )	c ( $\text{\AA}$ )							
0.0	5.878	23.050	3.921	689.6	29.25	5.11	3.10	65.0	66.18
0.5	5.879	23.051	3.921	689.9	28.29	5.19	3.18	63.4	66.77
1.0	5.882	23.053	3.919	690.7	32.46	5.26	3.24	62.4	57.02
1.5	5.886	23.055	3.917	691.7	27.42	5.33	3.34	60.0	65.61

concentration in hexaferrite. The crystallite size was calculated using Debye-Scherrer equation and the most intense peak (114) [14]. The crystallite size of yttrium substituted strontium hexaferrites increased in the range of 27 to 32 nm which was very small as compared to other hexaferrites [15, 16]. The X-ray density of the sample increased with x concentration and ranged from 5.11 to 5.33  $\text{g/cm}^3$ . The bulk density of prepared samples increased from 3.10 to 3.34  $\text{g/cm}^3$ . It was observed that the porosity of the sample decreased with the increase of  $\text{Y}^{3+}$  ion substitution in hexaferrite. The X-ray density, bulk density, porosity and specific surface area of all samples were calculated [17] as shown in Table I.

**Compositional analysis:** Fig. 2 shows the EDAX spectra of  $\text{SrY}_x\text{Fe}_{12-x}\text{O}_{19}$  samples sintered at 1000 °C for 6 h, wherein Fig. 2a  $x=0.0$  and in Fig. 2b  $x=1.5$ . The EDAX spectra

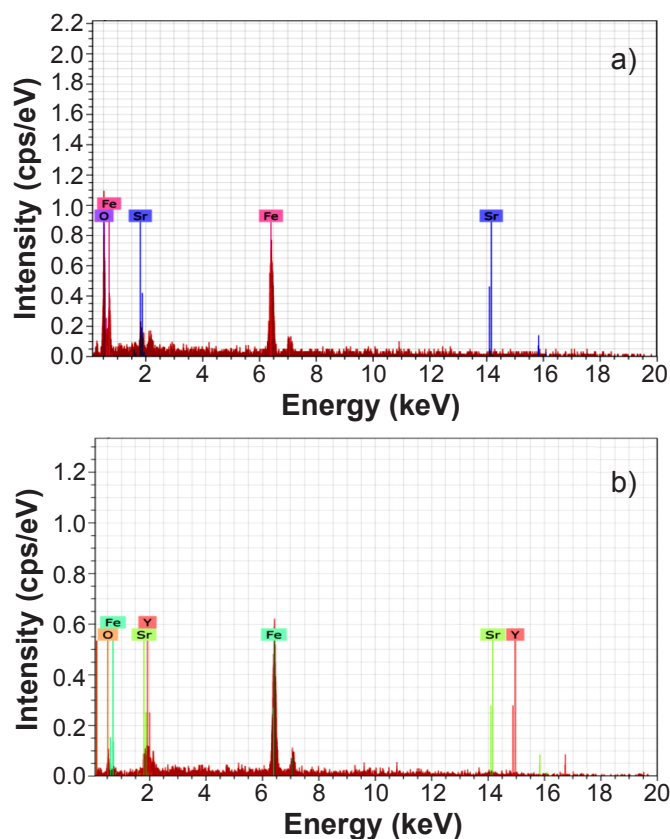


Figure 2: Energy-dispersive X-ray spectroscopy (EDAX) spectra of typical hexaferrite samples: a)  $x=0.0$ ; and b)  $x=1.5$ .

[Figura 2: Espectros de EDS de amostras típicas de hexaferrita: a)  $x=0,0$ ; e b)  $x=1,5$ .]

showed all peaks of their parent elements were present in the samples. They confirmed that only O, Fe, Sr and Y were present in the prepared samples and did not contain any kind of impurities. The observed compositions of both samples were approximately equal to the calculated stoichiometric proportional quantity.

**Morphological analysis:** Fig. 3 shows the FE-SEM morphology of  $\text{SrY}_x\text{Fe}_{12-x}\text{O}_{19}$  samples sintered at 1000 °C, wherein Fig. 3a  $x=0.0$  and in Fig. 3b  $x=1.5$ . The particle size was calculated by the linear intercept method; the observed

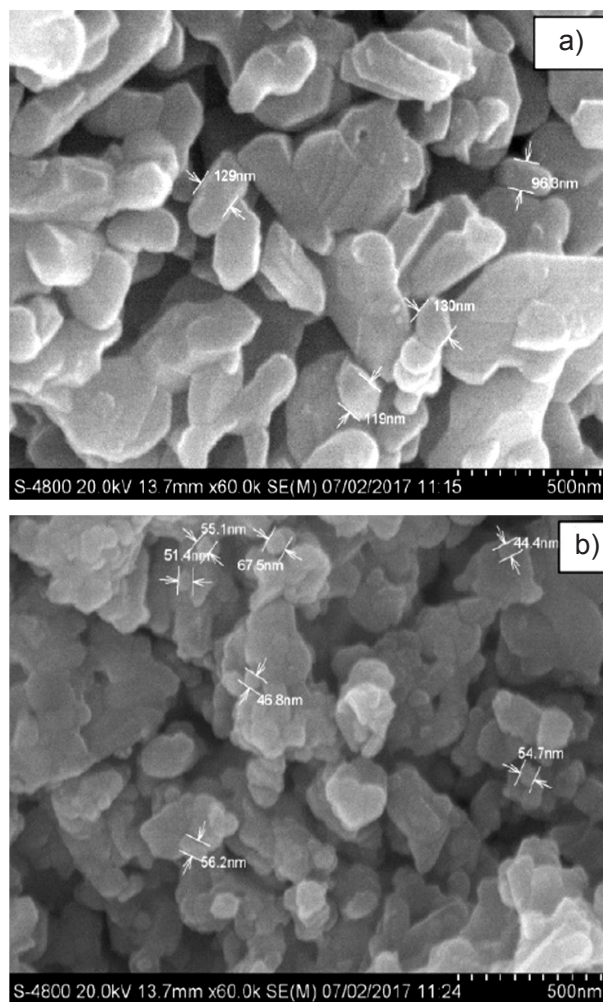


Figure 3: FE-SEM micrographs of the typical hexaferrite samples: a)  $x=0.0$ ; and b)  $x=1.5$ .

[Figura 3: Micrografias de MEV-FEG das amostras típicas de hexaferrita: a)  $x=0,0$ ; e b)  $x=1,5$ .]



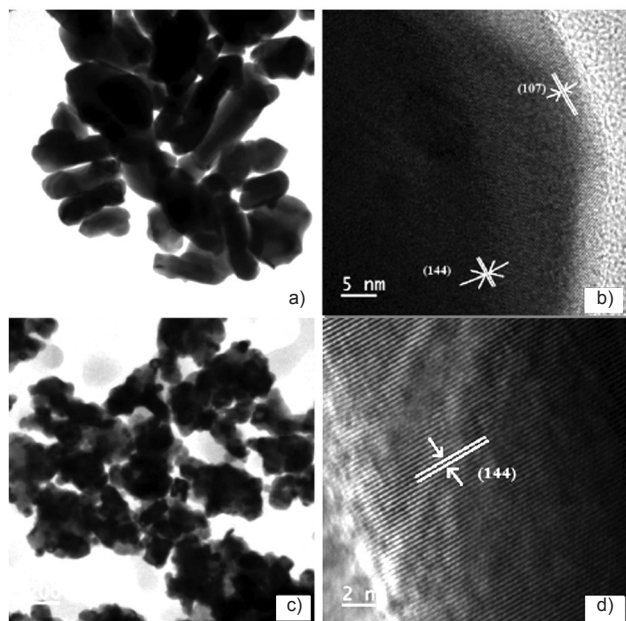


Figure 4: Bright field TEM (a,c) and HR-TEM (b,d) images for hexaferrite samples with  $x=0.0$  (a,b) and  $x=1.5$  (c,d); the obtained distance between the lattice fringes from high-magnification HR-TEM images (b,d) are 2.77 and 2.62 Å, respectively, which are in good agreement with the observed XRD planes (107) and (144).

[Figura 4: Imagens de campo claro de MET (a,c) e MET-AR (b,d) para amostras de hexaferrita com  $x=0,0$  (a,b) e  $x=1,5$  (c,d); a distância obtida entre as franjas de rede a partir das imagens de MET-AR de alta ampliação (b,d) é de 2,77 e 2,62 Å, respectivamente, as quais estão em concordância com os planos XRD observados (107) e (144).]

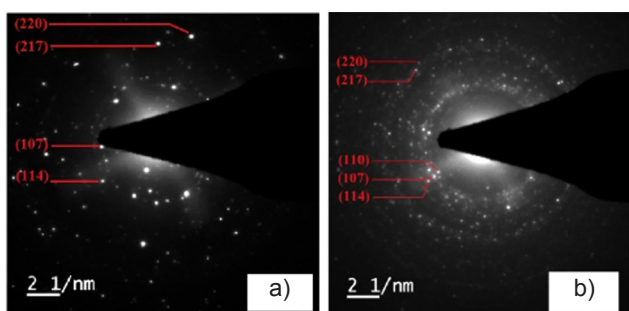


Figure 5: SAED patterns of  $\text{SrY}_x\text{Fe}_{12-x}\text{O}_{19}$  for: a)  $x=0.0$ ; and b)  $x=1.5$ .

[Figura 5: Padrões de difração de elétrons de área selecionada de  $\text{SrY}_x\text{Fe}_{12-x}\text{O}_{19}$  para: a)  $x=0,0$ ; e b)  $x=1,5$ .]

particle size was found between 90 and 130 nm for  $x=0.0$  and 44 and 70 nm for  $x=1.5$ . Many researchers report the values of particle size for hexaferrite in the range of 70 to 300 nm [18, 19]. In order to get more insight into the particle size, samples were characterized by HR-TEM. Fig. 4 shows the HR-TEM images of  $\text{SrY}_x\text{Fe}_{12-x}\text{O}_{19}$  sintered at 1000 °C for  $x=0.0$  and  $x=1.5$ . The particle size obtained by the HR-TEM was found to be 100-150 nm for  $x=0.0$  whereas it was difficult to measure the particle size for the  $x=1.5$  due to the agglomeration form of the particles. These values of particle size observed by FE-SEM and HR-TEM were not equal to

the values calculated by XRD; however, the overall trend of decreasing order in the particle size was maintained. Both FE-SEM and HR-TEM observation showed that the particle size decreased with the increase of  $\text{Y}^{3+}$  concentration in the strontium hexaferrite. The interplanar spacing was measured from lattice fringes in magnified images of HR-TEM; for  $x=0.0$  and 1.5 it was 2.77 and 2.62 Å, respectively, and these values agreed with the indexed family plane of (107) and (144). Fig. 5 shows the SAED (selected area electron diffraction) pattern of the pure and yttrium substituted strontium hexaferrites. The indexed planes (107) and (114) confirmed the formation of pure and substituted strontium hexaferrite.

**Magnetic properties:** Fig. 6 shows the room temperature magnetic hysteresis loops (M-H) of  $\text{SrY}_x\text{Fe}_{12-x}\text{O}_{19}$  samples with the applied field of 1.5 tesla. The magnetic parameters such as saturation magnetization ( $M_s$ ), remanence magnetization ( $M_r$ ), coercivity ( $H_c$ ), and Bohr magneton number ( $n_B$ ) were studied using M-H loops. Fig. 7a shows the variation of saturation magnetization and coercivity with  $\text{Y}^{3+}$  ion concentration in hexaferrites. It was observed that the saturation magnetization decreased from 49.6 to 35.4 emu/g with the substitution of yttrium ions. The decrease in magnetization was due to the substitution of non-magnetic  $\text{Y}^{3+}$  ions in place of magnetic  $\text{Fe}^{3+}$  ions. The magnetic moment of  $\text{Y}^{3+}$  ions is 0  $\mu_B$  and preferentially occupy octahedral spin up crystallographic site. This site occupation of  $\text{Y}^{3+}$  in place of  $\text{Fe}^{3+}$  reduced the resultant magnetic moment that decreased the strength of superexchange interactions of  $\text{Fe}^{3+}\text{-O}^{2-}\text{-Fe}^{3+}$ . The distribution of  $\text{Fe}^{3+}$  ions at five different lattice sites 12k, 2a, 2b, 4f<sub>1</sub> and 4f<sub>2</sub> collectively gives the magnetic moment in M-type hexaferrite. The 2b (trigonal bipyramidal) and 12k and 4f<sub>2</sub> (octahedral) sites affect the magnetocrystalline anisotropy in the M-type hexaferrite [1, 2]. The substitution of non-magnetic  $\text{Y}^{3+}$  ions with magnetic  $\text{Fe}^{3+}$  ions (5  $\mu_B$ ) from the site whose spins are in the upward direction reduced the saturation magnetization of the compositions with yttrium. The coercivity of the samples increased from 4889 to 6152 Oe with the increase of yttrium concentration in the strontium hexaferrite. The coercivity mainly depends upon the particle size and magnetocrystalline anisotropy. The particle size reduced with the substitution of yttrium which was attributed to the increase of the coercivity, and also the increase of the magnetocrystalline anisotropy which enhanced the coercivity. Fig. 7b shows the variation of remanence magnetization ( $M_r$ ) and remanence ratio ( $R=M_r/M_s$ ) with  $\text{Y}^{3+}$  ion concentration in  $\text{SrY}_x\text{Fe}_{12-x}\text{O}_{19}$ . The remanence magnetization was reduced from 29.01 to 17.65 emu/g, and its decreasing trend was the same as saturation magnetization. The Bohr magneton number ( $n_B$ ) of the prepared samples was calculated using Eq. A and values of saturation magnetization ( $M_s$ ) obtained from the hysteresis loop and molecular weight (MW) [20]. The values of Bohr magneton number with different composition of yttrium are summarized in Table II. It was observed that  $n_B$  decreased with the increase in  $\text{Y}^{3+}$  ion concentration in strontium hexaferrite. As the Bohr magneton number is directly related

to the saturation magnetization, shrinkage in  $M_s$  with yttrium lowered the Bohr magneton number.

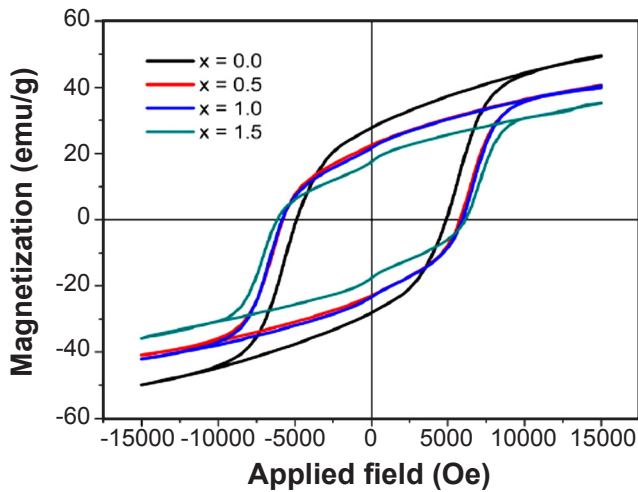


Figure 6: Room temperature M-H loops of  $\text{SrY}_x\text{Fe}_{12-x}\text{O}_{19}$  samples. [Figura 6: Ciclos de histerese (loops) M-H à temperatura ambiente de amostras de  $\text{SrY}_x\text{Fe}_{12-x}\text{O}_{19}$ .]

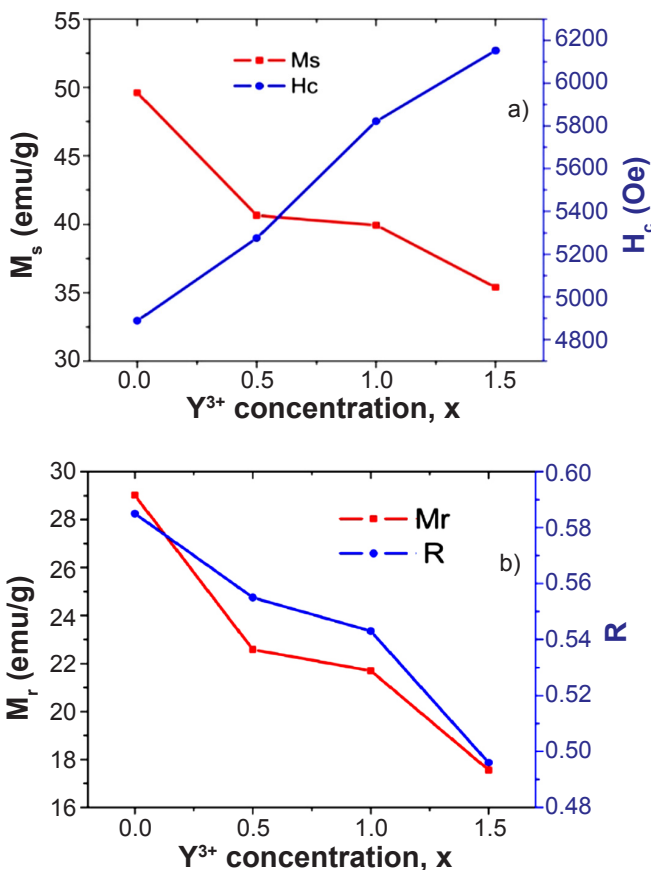


Figure 7: Variation of saturation magnetization,  $M_s$ , coercivity,  $H_c$  (a), remanence magnetization,  $M_r$ , and remanence ratio,  $R$  (b), with  $\text{Y}^{3+}$  substitution concentration in  $\text{SrY}_x\text{Fe}_{12-x}\text{O}_{19}$ . [Figura 7: Variação da magnetização de saturação,  $M_s$ , coercividade,  $H_c$  (a), magnetização remanente,  $M_r$ , e razão de remanência,  $R$  (b), com a concentração de substituição de  $\text{Y}^{3+}$  em  $\text{SrY}_x\text{Fe}_{12-x}\text{O}_{19}$ .]

$$n_b = \frac{MW.M_s}{5585} \quad (\text{A})$$

Table II - Saturation magnetization ( $M_s$ ), coercivity ( $H_c$ ), remanence magnetization ( $M_r$ ), magneton number ( $n_b$ ), and remanence ratio ( $R$ ) for  $\text{SrY}_x\text{Fe}_{12-x}\text{O}_{19}$  samples.

[Tabela II - Magnetização de saturação ( $M_s$ ), coercividade ( $H_c$ ), magnetização remanente ( $M_r$ ), número de magnétons de Bohr ( $n_b$ ) e razão de remanência ( $R$ ) para amostras de  $\text{SrY}_x\text{Fe}_{12-x}\text{O}_{19}$ .]

Conc. x	$M_s$ (emu/g)	$H_c$ (Oe)	$M_r$ (emu/g)	$n_b$	R
0.0	49.60	4889	29.01	9.43	0.585
0.5	40.65	5276	22.58	7.85	0.555
1.0	39.94	5822	21.70	7.83	0.543
1.5	35.40	6152	17.56	7.04	0.496

**Dielectric measurement:** the real and imaginary part of the dielectric constant was measured for  $\text{SrY}_x\text{Fe}_{12-x}\text{O}_{19}$  samples in the frequency range from 50 Hz to 5 MHz and is shown in Figs. 8a and 8b. The frequency dependence of the dielectric constant for all samples was measured at room temperature. It was observed that for all compositions the real and imaginary part of the dielectric constant decreased rapidly at the low-frequency range and became almost constant at the higher frequency region. This type of behavior in ferrites was according to the Maxwell-Wagner effect [21]. According to this theory, the assembly of ferrites is assumed to be made up of two layers: in the first conducting layer resides a large number of grains and in the second layer resides grain boundaries which are poor conductors. The polarization process in ferrites is similar to that of the conduction process, i.e. by electron transfer between ferric ( $\text{Fe}^{3+}$ ) and ferrous ( $\text{Fe}^{2+}$ ) ions. The electron transfer process between ferric ( $\text{Fe}^{3+}$ ) and ferrous ( $\text{Fe}^{2+}$ ) ions cannot follow the externally applied alternating electric field, due to the decrease in polarization with frequency. The voids, dislocations and other defects result in higher values of dielectric constant at low frequency. The values of the dielectric constant and ac conductivity are presented in Table III. The value of dielectric constant ( $\epsilon'$ ) of pure strontium hexaferrite was higher than the yttrium substituted strontium hexaferrite. The replacement of  $\text{Fe}^{3+}$  ions by  $\text{Y}^{3+}$  ions changed the conduction mechanism due to this dielectric constant decrease. Fig. 8c shows the variation of dielectric loss tangent ( $\tan\delta$ ) with frequency of  $\text{SrY}_x\text{Fe}_{12-x}\text{O}_{19}$  samples in real part for  $x = 0, 0.5, 1, 1.5$ . Initially, it was observed that the dielectric loss tangent decreased (except for  $x=0.0$ ) with the increase of frequency and a maximum peak appeared in the dielectric tangent loss. This was due to the resonance phenomenon; the natural frequency of jumping ions exactly matched with the frequency of the externally applied field. The ac conductivity of all samples of the yttrium substituted strontium hexaferrites was calculated

using the dielectric data and the relation given by Eq. B. Fig. 9 shows the variation of ac conductivity with the frequency of SrY<sub>x</sub>Fe<sub>12-x</sub>O<sub>19</sub> samples at room temperature. The ac conductivity of all samples increased with increasing frequency, since the ac conductivity of the sample was directly proportional to the angular frequency (ω) of the applied electric field. The transportation phenomenon of electrons via Fe<sup>2+</sup>/Fe<sup>3+</sup> ions at adjacent layers gives the conductivity in hexaferrite. The

ac conductivity increases at higher frequencies due to the decrease in the space charge polarization.

$$\sigma_{ac} = \omega \cdot \epsilon_0 \cdot \epsilon'' \tag{B}$$

Table III - Dielectric constant (ε'), ac conductivity (σ<sub>ac</sub>), resistivity (ρ), transition temperature (T<sub>M.S</sub>), and activation energy (ΔE) for SrY<sub>x</sub>Fe<sub>12-x</sub>O<sub>19</sub> samples.

[Tabela III - Constante dielétrica (ε'), condutividade ca (σ<sub>ac</sub>), resistividade (ρ), temperatura de transição (T<sub>M.S</sub>) e energia de ativação (E) para amostras de SrY<sub>x</sub>Fe<sub>12-x</sub>O<sub>19</sub>.]

Conc. x	ε'	σ <sub>ac</sub> (S/cm)	ρ x10 <sup>6</sup> (Ω.cm)	T <sub>K</sub> (K)	ΔE (eV)
0.0	130.35	9.02x10 <sup>-7</sup>	3.22	403	0.421
0.5	42.20	3.05x10 <sup>-7</sup>	8.10	408	0.514
1.0	43.53	4.11x10 <sup>-7</sup>	19.44	414	0.634
1.5	67.56	1.11x10 <sup>-6</sup>	48.76	418	0.783

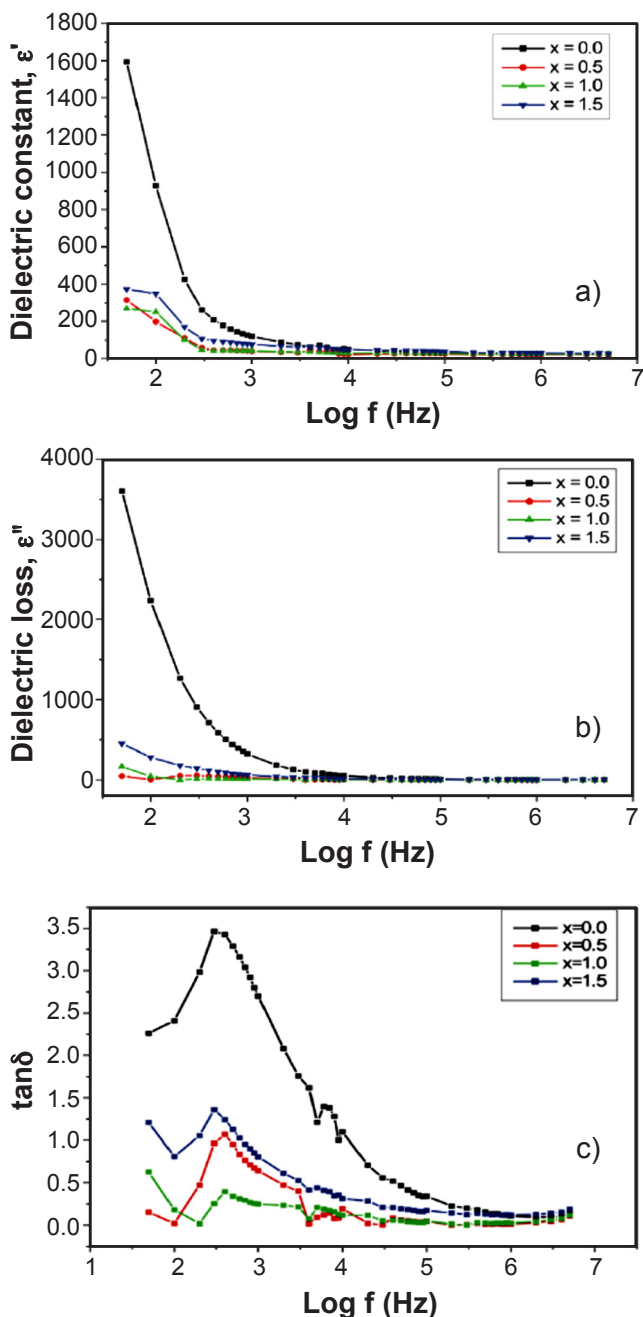


Figure 8: Variation of dielectric constant, ε' (a), dielectric loss, ε'' (b), and dielectric loss tangent, tanδ (c), with the frequency, f, for SrY<sub>x</sub>Fe<sub>12-x</sub>O<sub>19</sub> samples.

[Figura 8: Variação da constante dielétrica, ε' (a), perda dielétrica, ε'' (b) e tangente de perda dielétrica, tanδ (c), com a frequência, f, para amostras de SrY<sub>x</sub>Fe<sub>12-x</sub>O<sub>19</sub>.]

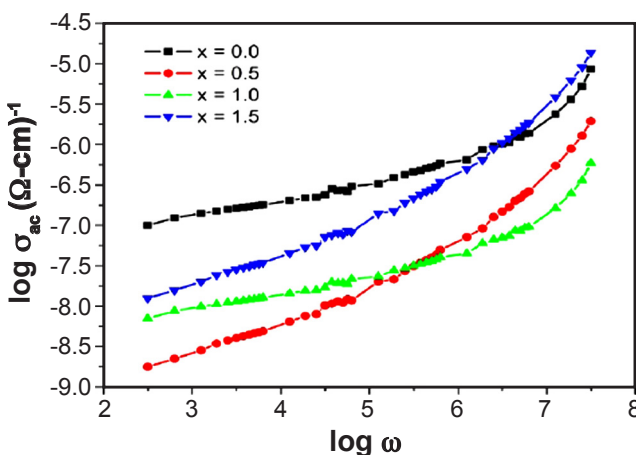


Figure 9: Variation of ac conductivity (σ<sub>ac</sub>) as a function of angular frequency (ω) for SrY<sub>x</sub>Fe<sub>12-x</sub>O<sub>19</sub> samples.

[Figura 9: Variação da condutividade CA (σ<sub>ac</sub>) em função da frequência angular (ω) para amostras de SrY<sub>x</sub>Fe<sub>12-x</sub>O<sub>19</sub>.]

**Electrical resistivity:** the electrical dc resistivity of samples was investigated by using the two-probe technique within the temperature range of 360 to 775 K. Fig. 10a shows the variation of electrical dc resistivity with temperature of SrY<sub>x</sub>Fe<sub>12-x</sub>O<sub>19</sub> samples for x= 0, 0.5, 1, 1.5. It was observed that the dc resistivity for all samples decreased with increasing the temperature. The dc resistivity became constant at higher temperatures for all samples. This behavior indicated the semiconducting nature of the samples. Here, the drift mobility of the charge carrier increased, i.e. electrons and holes decreased the dc electrical resistivity with temperature [22]. The values of dc resistivity with yttrium composition are given in Table III. The dc resistivity increased with yttrium concentration in strontium hexaferrite. The order of resistivity is 10<sup>7</sup> Ω.cm which is smaller than the Zr-Cu substituted strontium hexaferrite nanoparticles reported in [23]. The increase in dc resistivity



was attributed to the decrease in conductivity resulting from the electron hopping between the  $\text{Fe}^{3+}$  and  $\text{Fe}^{2+}$  ions [24]. The electron hopping between the  $\text{Fe}^{3+}$  and  $\text{Fe}^{2+}$  ions decreased due to the replacement of  $\text{Fe}^{3+}$  ions by the  $\text{Y}^{3+}$  ions. Also, the dc resistivity depends on other factors like the lattice parameter, grain size, voids, etc. [10, 25]. As the lattice parameter increased with the substitution of  $\text{Y}^{3+}$  ions due to the increase of inter-ionic distances in the strontium hexaferrite, this increased the barrier height for the hopping mechanism. Thus, electrical resistivity increased with the substitution of yttrium in strontium hexaferrite. The relation between electrical dc resistivity and the absolute temperature  $T$  is given by the Arrhenius relation:

$$\sigma = \rho_0 e^{\left(\frac{-E_g}{kT}\right)} \quad (\text{C})$$

where  $E_g$  is the activation energy and  $k$  is Boltzmann constant. Fig. 10b shows the variation of dc resistivity with the reciprocal of temperature of  $\text{SrY}_x\text{Fe}_{12-x}\text{O}_{19}$  samples. These plots showed a maximum at a particular temperature which corresponded to the transition of metal to semiconducting nature called metal-semiconductor transition temperature,

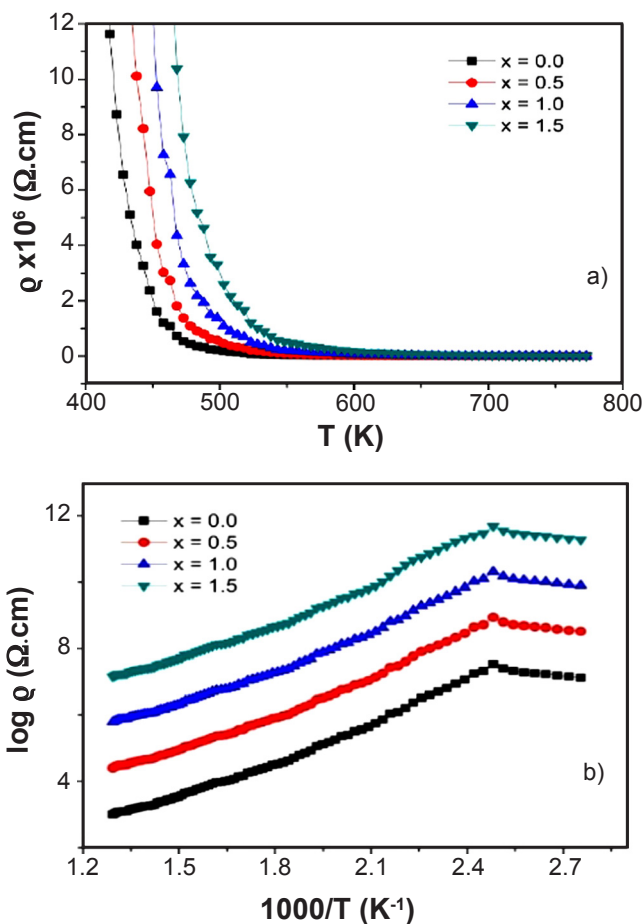


Figure 10: Variation of dc resistivity with temperature (a), and corresponding Arrhenius plot (b) for  $\text{SrY}_x\text{Fe}_{12-x}\text{O}_{19}$  samples. [Figura 10: Variação da resistividade CC com a temperatura (a) e correspondente gráfico de Arrhenius (b) para amostras de  $\text{SrY}_x\text{Fe}_{12-x}\text{O}_{19}$ .]

$T_{M-S}$ . Above the  $T_{M-S}$ , the conductivity showed metallic behavior and below the  $T_{M-S}$  semiconductor behavior. The value of transition temperature increased with the substitution concentration of  $\text{Y}^{3+}$  in strontium hexaferrite (Table III). The values of the activation energy measured from the Arrhenius plot in the semiconducting region are summarized in Table III. The activation energy increased from 0.421 to 0.783 eV which was similar to other reported study [24]. The increasing trend of activation energy was due to the increase in electrical dc resistivity with increasing yttrium concentration in strontium hexaferrite.

## CONCLUSIONS

$\text{Y}^{3+}$  substituted strontium hexaferrites were successfully synthesized by the sol-gel auto-combustion method. The XRD patterns confirmed the formation of a single phase of pure and substituted strontium hexaferrite. The lattice parameters  $a$  and  $c$  increased with the yttrium substitution content due to the difference in ionic radii of  $\text{Fe}^{3+}$  and  $\text{Y}^{3+}$  ions. The grain size decreased with yttrium substitution as observed from FE-SEM analysis. The interplanar distances obtained from the magnified HR-TEM images were in good agreement with the XRD indexed planes, confirming the formation of pure and substituted hexaferrite. The saturation magnetization decreased whereas the coercivity increased with the substitution of  $\text{Y}^{3+}$  ions in hexaferrite. The dielectric constant ( $\epsilon'$ ) and dielectric loss tangent ( $\tan \delta$ ) decreased whereas the electrical dc resistivity and its activation energy increased with the substitution concentration of yttrium. All dielectric parameters were in good agreement with the electrical dc resistivity parameters.

## REFERENCES

- [1] M.N. Ashiq, M.J. Iqbal, I.H. Gul, J. Magn. Mater. **323** (2011) 259.
- [2] M.J. Iqbal, M.N. Ashiq, P.H. Gomez, J. Alloys Compd. **478** (2009) 736.
- [3] I. Auwal, H. Erdemi, H. Sözeri, H. Güngüneş, A. Baykal, J. Magn. Mater. **412** (2016) 69.
- [4] L. Lechevallier, J. Le Breton, J. Magn. Mater. **290** (2005) 1237.
- [5] G.M. Rai, M. Iqbal, K. Kubra, J. Alloys Compd. **495** (2010) 229.
- [6] I. Gul, F. Amin, A. Abbasi, M. Anis-ur-Rehman, A. Maqsood, Scr. Mater. **56** (2007) 497.
- [7] P. Bercoff, C. Herme, S. Jacobo, J. Magn. Mater. **321** (2009) 2245.
- [8] F. Ghanbari, A. Arab, M.S. Bor, M. Mardaneh, J. Electr. Mater. **46** (2017) 2112.
- [9] T.T.V. Nga, N.P. Duong, T.D. Hien, J. Magn. Mater. **324** (2012) 1141.
- [10] A. Thakur, R. Singh, P. Barman, J. Magn. Mater. **326** (2013) 35.
- [11] Q. Fang, H. Cheng, K. Huang, J. Wang, R. Li, Y. Jiao, J. Magn. Mater. **294** (2005) 281.

- [12] D.A. Vinnik, D.A. Zherebtsov, L.S. Mashkovtseva, S. Nemrava, N.S. Perov, A.S. Semisalova, I.V. Krivtsov, L.I. Isaenko, G.G. Mikhailov, R. Niewa, *Cryst. Growth Des.* **14** (2014) 5834.
- [13] I. Auwal, B. Ünal, A. Baykal, U. Kurtan, M. Amir, A. Yildiz, M. Sertkol, *J. Supercond. Novel Magn.* **30** (2017) 1813.
- [14] R.H. Kadam, A.A. Birajdar, S.T. Alone, S.E. Shirsath, *J. Magn. Magn. Mater.* **327** (2013) 167.
- [15] R. Parker, in *Proc. ICF-3* (1980) 375.
- [16] S.W. Lee, S.Y. An, I.-B. Shim, C.S. Kim, *J. Magn. Magn. Mater.* **290** (2005) 231.
- [17] H. Luo, B. Rai, S. Mishra, V. Nguyen, J. Liu, *J. Magn. Magn. Mater.* **324** (2012) 2602.
- [18] G. Mu, N. Chen, X. Pan, H. Shen, M. Gu, *Mater. Lett.* **62** (2008) 840.
- [19] M. Radwan, M. Rashad, M. Hessien, *J. Mater. Proc. Techn.* **181** (2007) 106.
- [20] R.H. Kadam, K. Desai, V.S. Shinde, M. Hashim, S.E. Shirsath, *J. Alloys Compd.* **657** (2016) 487.
- [21] Y. Bakış, I. Auwal, B. Ünal, A. Baykal, *Compos. Part B Eng.* **99** (2016) 248.
- [22] M.N. Ashiq, S. Shakoore, M. Najam-ul-Haq, M.F. Warsi, I. Ali, I. Shakir, *J. Magn. Magn. Mater.* **374** (2015) 173.
- [23] M.J. Iqbal, M.N. Ashiq, *Chem. Eng. J.* **136** (2008) 383.
- [24] M.J. Iqbal, M.N. Ashiq, P. Hernandez-Gomez, J.M. Munoz, *Scr. Mater.* **57** (2007) 1093.
- [25] R. Sharma, S. Singhal, *Physica B Condens. Matter.* **414** (2013) 83.
- (*Rec. 22/08/2018, Rev. 15/10/2018, 20/11/2018, 16/01/2019, Ac. 17/01/2019*)

